Rate enhancement by Cu in NixCu1-x/ZrO2 bimetallic catalysts for hydrodeoxygenation of stearic acid

Catalysis Science & Technology

ARTICLE

Rate enhancement by Cu in Ni_xCu_{1-x}/ZrO_2 bimetallic catalysts for hydrodeoxygenation of stearic acid

Christoph Denk,[a] Sebastian Foraita,[a] Libor Kovarik,[b,c] Kelsey Stoerzinger,[b,d] Yue Liu,[a] Eszter Baráth*[a] and Johannes A. Lercher*[a,b]

Hydrodeoxygenation of stearic acid on Ni/ZrO_2 to *n*-heptadecane occurs via the reduction to octadecanal, followed by decarbonylation of the aldehyde to *n*-heptadecane. Stearic acid binds stronger than 1-octadecanal on Ni, causing decarbonylation to start only once stearic acid is almost fully converted. This first step is enhanced by addition of Cu either in the form of Cu/ZrO_2 or in the form of a ZrO_2 supported Ni_xCu_{1-x} nano-alloy. Cu has not only a higher activity for the reduction of stearic acid, it also increases the activity of Ni for decarbonylation of 1-octadecanal by increasing the electron density of Ni in the bimetal catalyst. The combination of these two effects leads to high activity of Ni-Cu bimetallic catalysts.

Introduction

Hydrodeoxygenation (HDO) of fatty acids and their triglyceride esters is a potentially important route to high quality distillate fuels.[1-3] Such a process needs to saturate double bonds, as well as to reduce the acid function to the corresponding equilibrated aldehydes and alcohols, which are decarbonylated and dehydrated, respectively. The relative abundance of hydrogenating and acid-base functions determines whether hydrodeoxygenation occurs via dehydration[4,5] or decarbonylation.[4,5]

Suitable catalysts for HDO of fatty acids include transition metals, metal phosphides and sulfides. The support also accelerates reaction rates by introducing redundant pathways for reduction and deoxygenation steps.[1-3,6] ZrO_2 has been found to be a particularly suitable support,[5] because oxygen defects are instrumental for the reactive chemisorption of fatty acids. The higher defect concentration of monoclinic (*m*-ZrO_2) compared to tetragonal ZrO_2 (*t*-ZrO_2), for example, leads to a significantly higher catalytic activity.[5a] Addition of SiO_2 to ZrO_2 on the other hand creates Brønsted acidity, which in turn enhances dehydration over decarbonylation.[7]

While earth abundant transition metals, such as Ni, have been explored as economic and suitable catalysts,[8] the parent metal catalysts require modifications to enhance the catalytic activity, tailoring both, the specific activity transferring hydrogen, as well as the binding of the acid.[9-11] Preliminary experiments have shown promising properties when Ni was combined with Cu in the active metal phase.

Ni-Cu alloys are classified as weakly exothermic,[12] with both partners largely retaining their individual electronic properties.[12] Mutual electronic influence is typically attributed to a reduction of the d-band width and a redistribution of the d-band electrons. Difference in the oxophilicity of the alloy constituents; charge differences between them strengthens the interactions with polar groups.[13] It is interesting to note that Cu supported on transition metal oxides has been reported to be an efficient catalyst for the selective reduction of acids to alcohols.[14-18]

Here we report the combination of Cu and Ni in bimetallic catalysts supported on ZrO_2. The presence of Cu enhances the stearic acid reduction and the formation of Ni_xCu_{1-x} nano-alloys increases decarbonylation rate via an electronic promotion of Ni, leading to higher rates of HDO.

Results and Discussion

Catalyst physicochemical properties

ZrO_2 supported Ni-Cu bimetallic catalysts with different Ni/Cu ratios (labeled as Ni_xCu_{1-x}) were prepared by wet impregnation. The labeling of x represents the atomic fraction of the two elements. The physicochemical properties of the five catalysts are compiled in Table 1. All catalysts had the same specific surface area (84 ± 3) m^2 g^{-1}, very similar acid and base site concentrations of 0.19 ± 0.04 mmol g^{-1} and 0.27 ± 0.02 mmol g^{-1}, respectively, indicating that the support[19] was hardly modified by the metal deposition (Table 1). Zirconia was monoclinic (XRD peaks at 24.5°, 28.3°, 31.6°, 34.5°, 35.3° and 40.7°, JCPDS card No. 37-1484)[20] (ESI†, **Fig. S1**). A small shoulder at 30.2° suggests a minor tetragonal fraction (JCPDS card No. 17-0923).[21]. For Ni/ZrO_2, the average metal particle size was 20 nm, estimated from widths of the Ni(111) at 44.6° and Ni(200)

[a] *Department of Chemistry and Catalysis Research Center, Technische Universität München Lichtenbergstraße 4, 85747 Garching (Germany)*
E-mail: eszter.barath@tum.de, johannes.lercher@ch.tum.de
[b] *Institute for Integrated Catalysis, Pacific Northwest National Laboratory 902 Battelle Boulevard, Richland, WA 99352 (USA)*
[c] *Environmental Molecular Sciences Laboratory, Pacific Northwest National Laboratory, Richland, WA 99352 (USA)*
[d] *Physical and Computational Sciences Directorate, Pacific Northwest National Laboratory, Richland, Washington WA 99352 (USA)*
† Electronic Supplementary Information (ESI). See DOI: 10.1039/x0xx00000x

This journal is © The Royal Society of Chemistry 20xx

Catal. Sci. Technol., 2019, **00**, 1-3 | **1**

at 51.9° diffraction peak (JCPDS 04-0850) (ESI†, **Fig. S1**). The fraction of exposed Ni determined by H_2-chemisorption was 3.5%.

Table 1 Physicochemical properties of bimetallic Ni_xCu_{1-x}/ZrO_2 catalysts

Catalyst [a]	S_{BET} $(m^2\ g^{-1})$	Ni-loading [b] (wt%)	Cu-loading [b] (wt%)	$r_{ex.surf}$ [c] (%)	Concentration of acid sites [d] $(mmol\ g^{-1})$	Concentration of basic sites [e] $(mmol\ g^{-1})$
Ni/ZrO_2	82	10	0	3.5	0.19	0.28
$Ni_{0.79}Cu_{0.21}/ZrO_2$	81	7.5	2.1	1.5	0.23	0.27
$Ni_{0.59}Cu_{0.41}/ZrO_2$	87	5.6	4.2	1.8	0.23	0.27
$Ni_{0.29}Cu_{0.71}/ZrO_2$	83	2.5	6.5	2.8	0.16	0.25
Cu/ZrO_2	85	0	8.7	-	0.15	0.29

[a] Label according to molar ratio of Ni-Cu.
[b] Determined by Atomic Absorption Spectroscopy (AAS).
[c] $r_{ex.surf}$ ratio of exposed Ni surface, determined from H_2-Chemisorption.
[d] Determined by TPD of NH_3.
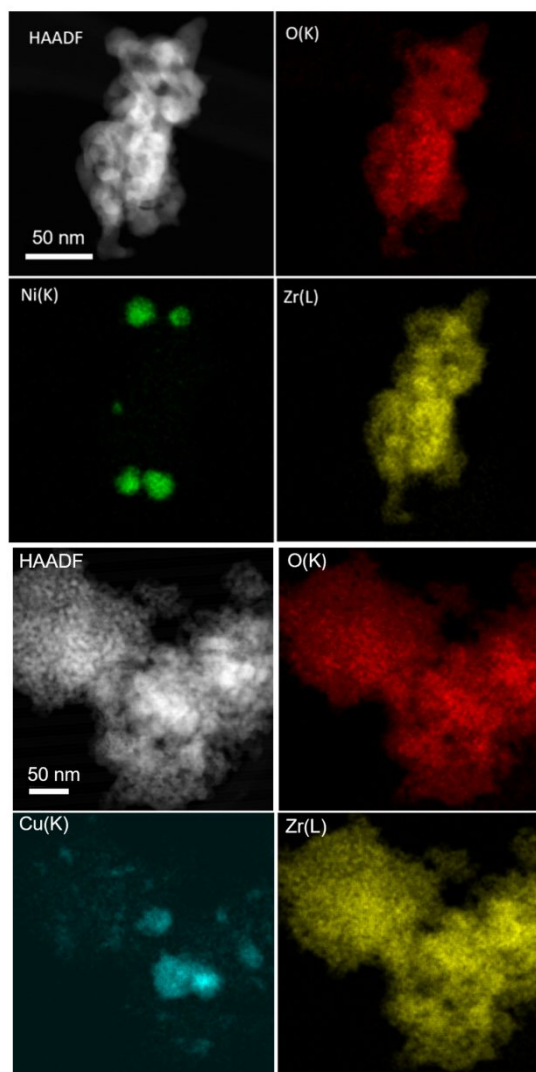[e] Determined by TPD of CO_2.

When adding a low concentration of Cu (Cu:Ni of 0.21:0.79) the H_2-uptake normalized to Ni was lower than for Ni/ZrO_2 (Table 1). In agreement with Ponec, the surface concentration of Ni was lower than the bulk concentration, and remained constant over a wide range of Ni_xCu_{1-x} compositions, indicating a slightly over-proportional surface concentration of Cu.[12d] At higher Cu concentrations (Cu:Ni of 0.71:0.29), Ni diffraction peaks were not observed and the fraction of exposed Ni increased to 2.8%,[22] while large Cu crystallites of 85 nm were observed as judged from the widths of the Cu(111) diffraction peak at 43.4° (JCPDS 04-0836) (ESI†, **Fig. S1**). It increased to an average diameter of more than 100 nm on Cu/ZrO_2.

On the bimetallic catalysts, Ni-Cu alloys were identified. **Fig. 1** shows the XRD pattern of the catalysts in the 2θ range of 42°-47°. The diffraction peaks of m-ZrO_2 support were subtracted to better visualize the diffraction peaks of the supported metal. Besides the peaks of Cu(111) at 43.4° (JCPDS 04-0836) and of Ni(111) at 44.6° (JCPDS 04-0850), a broad and shifted diffraction peak between them appeared on the Ni-Cu bimetallic samples, attributed to the Ni_xCu_{1-x} nano-alloy.[23] The large width at half height points to small domains of ordering in the alloyed phase.
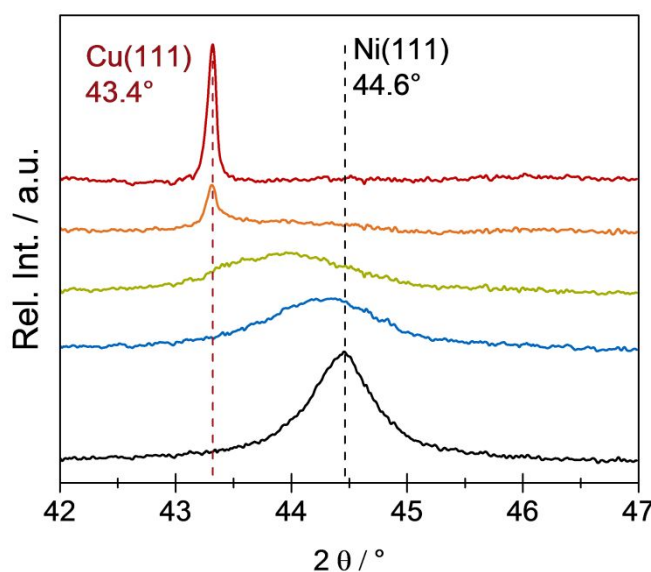

Fig. 1 XRD patterns of Ni_xCu_{1-x}/ZrO_2 (x = 1, 0.79, 0.59, 0.29, 0) catalysts by subtraction of the support m-ZrO_2 in the 2θ range 42–47°.

The spatially resolved elemental distributions of Ni/ZrO_2, Cu/ZrO_2 and Ni_xCu_{1-x}/ZrO_2 are compiled in **Fig. 2** and **Fig. 3**. On the monometallic Ni/ZrO_2 and Cu/ZrO_2, defined particles of Ni and Cu are visible, and the average diameter of Ni particles is smaller than that of Cu particles (**Fig. 2**). Zirconium is homogenously distributed over the whole agglomerates for all materials. The overlaying Ni and Cu distributions for bimetallic catalysts shows that they both coexist in each particle (**Fig. 3**). Small Cu and Ni subdomains were observed.

2 | *Catal. Sci. Technol*., 2019, **00**, 1-3

This journal is © The Royal Society of Chemistry 20xx

Fig. 2 STEM HAADF (scanning transmission electron microscopy high angle annular dark-field) images of Ni/ZrO_2, and Cu/ZrO_2 agglomerate used for energy dispersive spectroscopy (EDS) mapping (oxygen, zirconium and either nickel or copper).
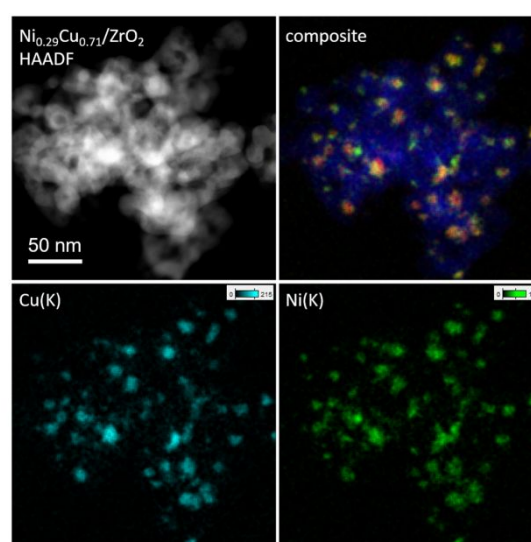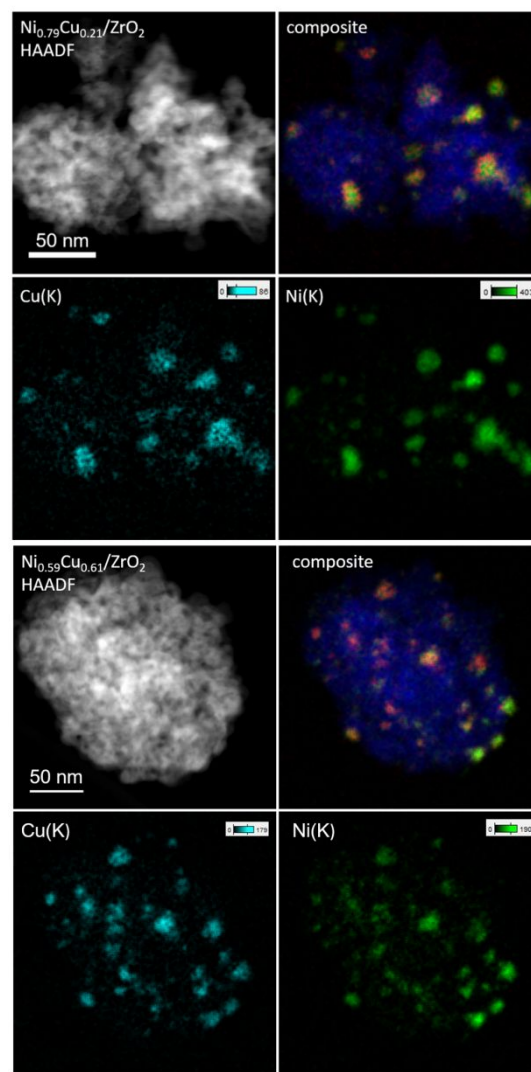
Fig. 3 STEM HAADF (scanning transmission electron microscopy high angle annular dark-field) images of Ni_xCu_{1-x}/ZrO_2 (x = 0.79, 0.59, 0.29) agglomerate used for energy dispersive spectroscopy (EDS) mapping zirconium, copper and nickel. In the composite image zirconium is blue, copper is red and nickel is green.

This journal is © The Royal Society of Chemistry 20xx

Catal. Sci. Technol., 2019, **00**, 1-3 | **3**

To characterize the mutual electronic influence between Ni and Cu, IR spectra of adsorbed CO (**Fig. 4**) and X-ray photoelectron spectra (XPS, **Fig. 5**) were used. In the IR spectra, Cu/ZrO_2 showed only a minor adsorption of CO, as judged from the very weak band at 2100 cm^{-1}.[22] For Ni/ZrO_2, the band at 2038 cm^{-1} is attributed to linearly bound CO on Ni^0,[24] the band at 1921 cm^{-1} to bridging CO. The intensity of the band of bridging CO decreased strongly in the presence of Cu, suggesting that Ni is well interdispersed with Cu.[12] Increasing the fraction of Cu led to a gradual redshift of the band of linearly adsorbed CO from 2019 via 2011 to 2004 cm^{-1}. This redshift indicates a stronger bond and an increase in the electron back donation for CO, indicating that Ni increased in electron density as the Cu concentration increased.[22,25,26]
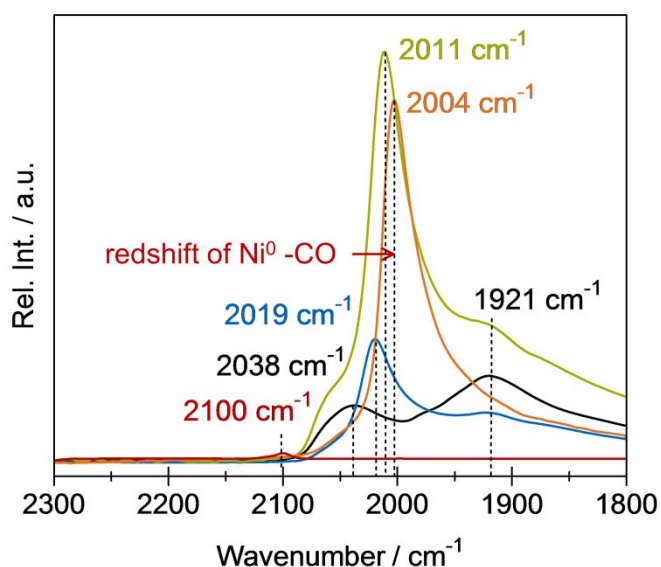
Fig. 4 IR spectra of CO adsorbed on Ni_xCu_{1-x}/ZrO_2 (x = 1, 0.79, 0.59, 0.29, 0) at 40°C. The adsorption of CO was performed at 0.3 mbar until equilibrium was reached, then evacuated (p = 10^{-7} mbar) for 5 min to remove physisorbed and gas phase CO. The IR spectra of adsorbed CO were normalized by the weight of Ni in the respective wafer.

Two representative catalysts $Ni_{0.29}Cu_{0.71}/ZrO_2$ (●) and $Ni_{0.79}Cu_{0.21}/ZrO_2$ (●) were characterized by X-ray photoelectron spectroscopy (**Fig. 5**). The $Cu_{2p3/2}$ binding energy was higher than for pure Cu (932.47 eV),[27] indicating that electron transfer from Cu to Ni occurred. The $Cu_{2p1/2}$ and $Cu_{2p3/2}$ binding energies were lowered by 0.3 eV with increasing Ni-content (x = 0.29 to 0.79). Thus, it was concluded that the electron density at Cu was lowered, while that of Ni was increased, in line with the redshift of the IR bands of adsorbed CO. In contrast to Cu, Ni was not fully reduced, hence, also binding energies for Ni^{2+} were found. The ratio of Ni^0 to Ni^{2+} was higher at higher Ni concentrations. This suggests that in presence of Cu small Ni particles may exist in $Ni_{0.29}Cu_{0.71}/ZrO_2$, which are hypothesized to be more easily oxidized than the Ni-rich alloyed particles. Ni in bimetallic particles had a $Ni_{2p3/2}$ binding energy of 852.1 eV, 0.5 eV lower than bulk Ni,[27] suggesting a higher electron density than in Ni/ZrO_2. Both shifts indicate that electron density at Cu was lower and that of Ni was higher than in monometallic catalysts (**Fig. 5**).
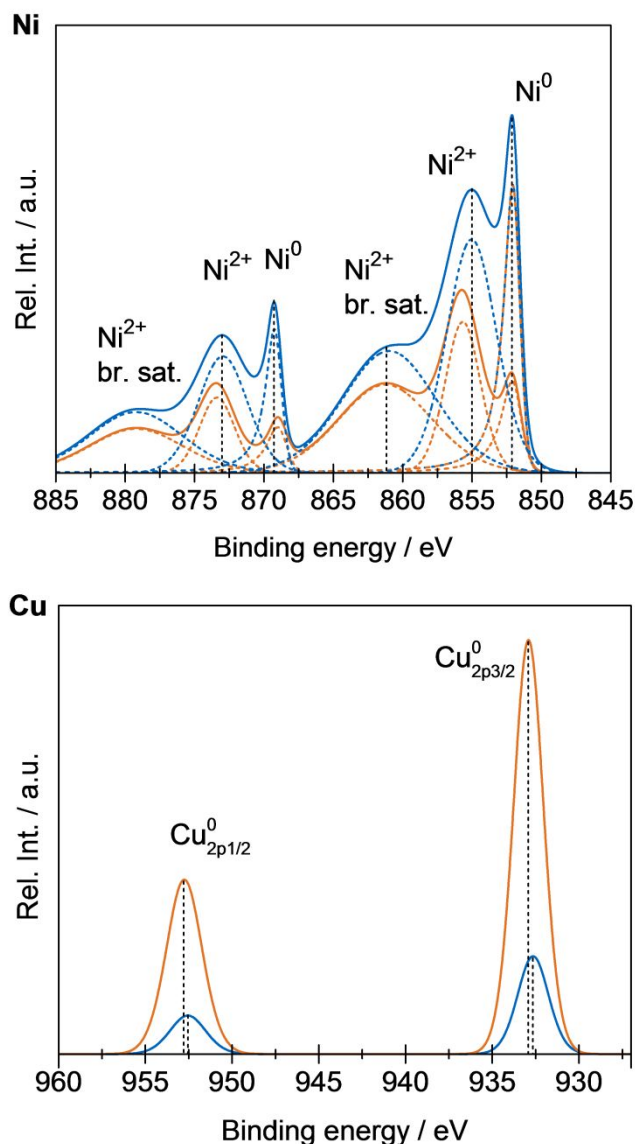

Fig. 5 XPS spectra for Ni_xCu_{1-x}/ZrO_2 (x = 0.29; 0.79) showing the binding energy of Cu and Ni (br. sat./ broad satellite).

Catalytic activity

Previous studies of stearic acid HDO have identified the reaction network shown in Scheme 1. The critical reaction is the reductive deoxygenation of the stearic acid to 1-octadecanal (Scheme 1/ **a**) followed by the decarbonylation to *n*-heptadecane (Scheme 1/ **b**). Hydrogenation of 1-octadecanal to 1-octadecanol (Scheme 1/ **c**) is fast and reversible. In presence of Brønsted acid sites, 1-octadecanol dehydrates to *n*-octadecene (Scheme 1/ **d**), which is in turn hydrogenated to *n*-octadecane (Scheme 1/ **e**). 1-Octadecanol also forms reversibly stearyl stearate with stearic acid (Scheme 1/ **f**).[4b,5,7] The two parallel pathways starting from 1-ocatadecanal lead to alkanes of different size: (i) decarbonylation to *n*-heptadecane (C_{17}), and (ii) hydrogenation to 1-octadecanol followed by dehydration and hydrogenation to *n*-octadecane (C_{18}). The reductive deoxygenation to 1-octadecanal is the slowest step on Ni/ZrO_2

4 | *Catal. Sci. Technol.*, 2019, **00**, 1-3

This journal is © The Royal Society of Chemistry 20xx

(Scheme 1/ step **a**)[4a] and a rate increase for this step is critical to achieve higher activity.
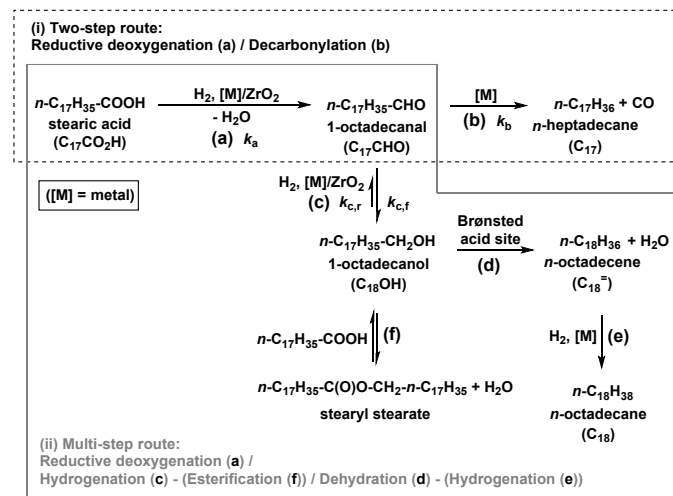
Scheme 1 Reaction network for the hydrodeoxygenation of stearic acid.[4b,5,7] k_a, k_b and $k_{c,f}$ and $k_{c,r}$ are referring to the corresponding rate constant values determined for step **a**, **b** and **c** (for detailed description see ESI†, **Eq.S1-Eq.S10**).

Cu and Ni have different catalytic activities for reductive deoxygenation of stearic acid (Scheme 1/ **a**) and decarbonylation of 1-octadecanal (Scheme 1/ **b**). Ni/ZrO$_2$ shows moderate activity for both reactions, while in contrast, Cu/ZrO$_2$ is highly active in the reductive acid deoxygenation, but hardly shows activity for decarbonylation (**Fig. 6**).
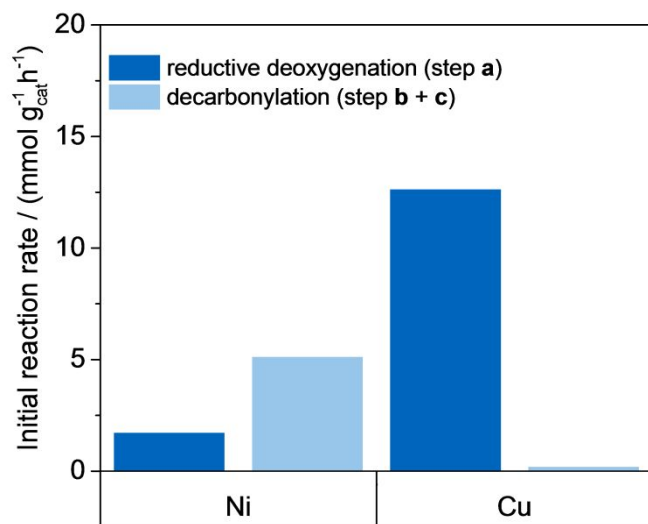
Fig. 6 Initial reaction rate for (**a**) the reductive deoxygenation of stearic acid on Ni/ZrO$_2$ and Cu/ZrO$_2$ and (**b** + **c**) decarbonylation reaction of 1-octadecanal. Reaction conditions: Stearic acid or 1-octadecanol (0.5 g), Ni/ZrO$_2$ or Cu/ZrO$_2$ (0.05 g), n-dodecane (100 mL), 260 °C, $p(H_2)$ = 40 bar, 600 rpm.

Indeed, HDO of stearic acid on Ni/ZrO$_2$ (**Fig. 7A**) showed that, 1-octadecanol and 1-octadecanal were formed as (pseudo) primary intermediates and n-heptadecane appeared as secondary product (**Fig. 7A**). On Cu/ZrO$_2$ stearic acid was rapidly reduced to 1-octadecanol (**Fig. 7B**). As the metal-oxygen bond dissociation enthalpy for Ni is higher than for Cu, we

hypothesize that O-species on Cu are less stable than that on Ni.[28] Hence, Cu nanoparticles offer a higher concentration of oxygen defects than Ni nanoparticles, leading to a higher rate of acid reduction on Cu. After 2 h on Cu/ZrO$_2$ 1-octadecanol and 1-octadecanal were equilibrated with a ratio of 230 (c(C$_{18}$OH)/c(C$_{17}$CHO) at 40 bar H$_2$). Only traces of n-heptadecane and n-octadecane were formed.
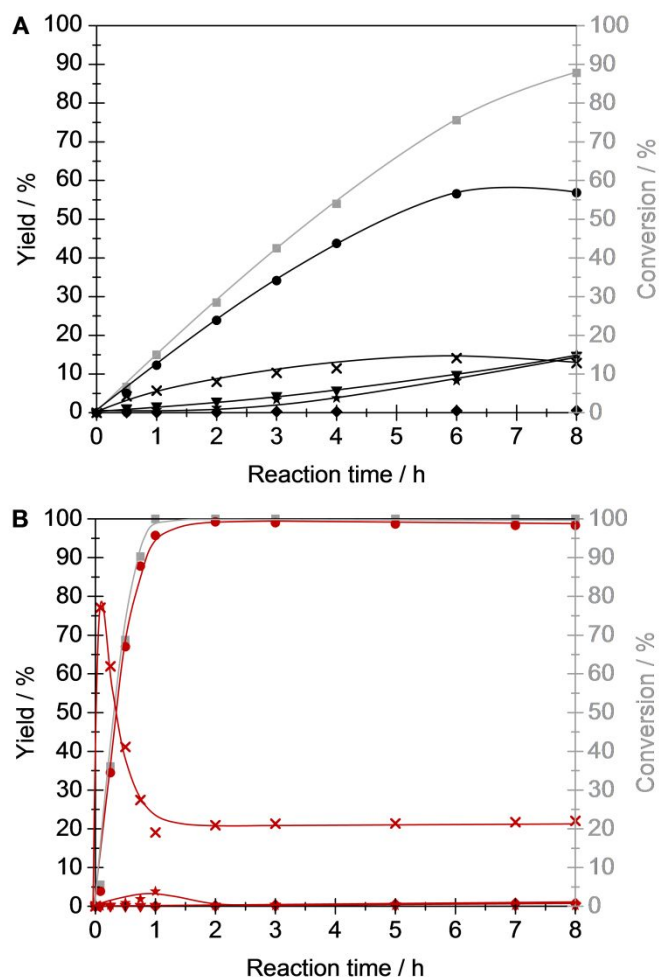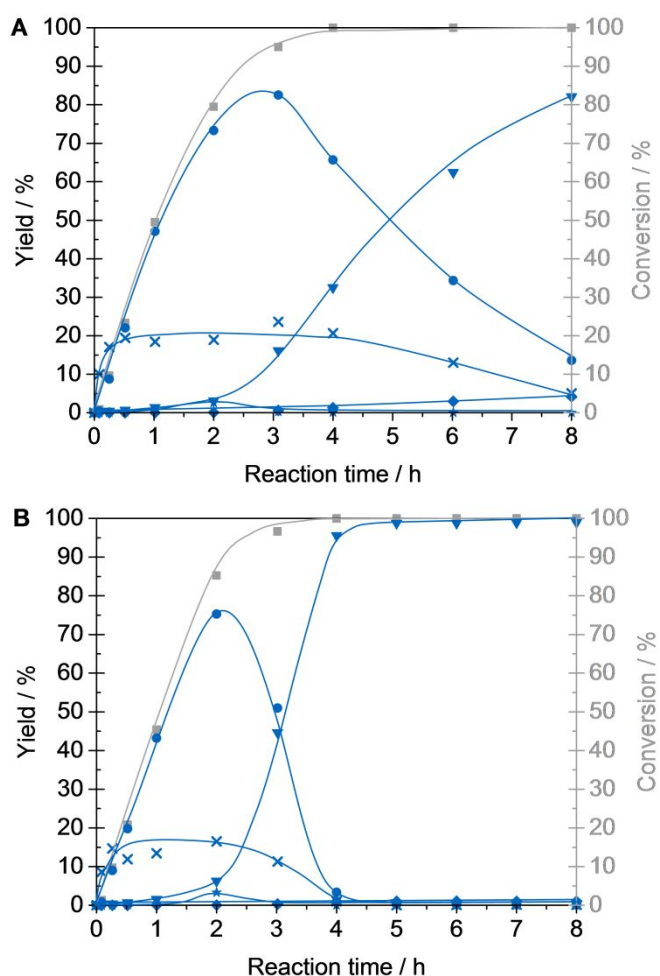

Fig. 7 Product distribution for the hydrodeoxygenation of stearic acid on Ni/ZrO$_2$ (**A**) and Cu/ZrO$_2$ (**B**) as a function of time. Conversion of stearic acid (■), yield of 1-octadecanol (●, ●), n-heptadecane (▼, ▼), n-octadecane (♦, ♦), 1-octadecanal (50 fold) (×, ×) and stearyl stearate (*, *). Reaction conditions: Stearic acid (0.5 g), Ni/ZrO$_2$ or Cu/ZrO$_2$ (0.2 g), n-dodecane (100 mL), 260 °C, $p(H_2)$ = 40 bar, 600 rpm.

A Ni-Cu bimetallic catalyst is, thus, hypothesized to combine the high activity of Cu for the reduction of stearic acid to 1-octadecanal (Scheme 1/ **a**) and the ability of Ni for decarbonylation of 1-octadecanal to n-heptadecane (Scheme 1/ **b**). Let us compare now the Ni$_x$Cu$_{1-x}$/ZrO$_2$ and a physical mixture of Ni/ZrO$_2$ and Cu/ZrO$_2$ as the reference.

HDO of stearic acid on Ni-Cu nano-alloys
Using the physical mixture of 0.79 Ni/ZrO$_2$ and 0.21 Cu/ZrO$_2$ (**Fig. 8A**) and the respective alloy Ni$_{0.79}$Cu$_{0.21}$/ZrO$_2$ (**Fig. 8B**) resulted in the rapid conversion of stearic acid to 1-octadecanol as primary product for both catalysts, independently if the

This journal is © The Royal Society of Chemistry 20xx

Catal. Sci. Technol., 2019, **00**, 1-3 | **5**

Ni$_{0.79}$Cu$_{0.21}$ alloy or the physical mixture was used (**Fig. 8B**). Compared to the monometallic catalysts (Ni/ZrO$_2$ or Cu/ZrO$_2$), the overall formation of *n*-heptadecane was higher on both the 0.79 Ni/ZrO$_2$ + 0.21 Cu/ZrO$_2$ mixture and Ni$_{0.79}$Cu$_{0.21}$/ZrO$_2$. While *n*-heptadecane yield on Ni/ZrO$_2$ was only 15% and it was hardly converted on Cu/ZrO$_2$ after 8 h, the yield of *n*-heptadecane reached 82% after 8 h on 0.79 Ni/ZrO$_2$ + 0.21 Cu/ZrO$_2$ mixture and 100% readily after 4h on Ni$_{0.79}$Cu$_{0.21}$/ZrO$_2$. Analyzing the individual reaction steps, the reductive dehydrogenation rate of stearic acid on Ni$_{0.79}$Cu$_{0.21}$/ZrO$_2$ was similar to that on the physical mixture: stearic acid conversion of 85% after 2 h on the former and 80% on the later. In contrast, the decarbonylation of 1-octadecanal, represented by the formation rate of *n*-heptadecane, was much more efficient on Ni$_{0.79}$Cu$_{0.21}$/ZrO$_2$ than on the physical mixture.

lower rate to *n*-heptadecane compared to a Ni rich alloy (Ni$_{0.79}$Cu$_{0.21}$/ZrO$_2$, **Fig. 8B**). Full conversion to hydrocarbons was achieved on all three bimetallic catalysts. Ni$_{0.59}$Cu$_{0.41}$/ZrO$_2$ combines a moderate acid reduction rate with the highest decarbonylation rate, thus, the fastest production of *n*-heptadecane. This catalyst can be fully recycled, reaction rates declined only slightly over three cycles and the selectivity changed only marginally (ESI†, **Fig. S2**).
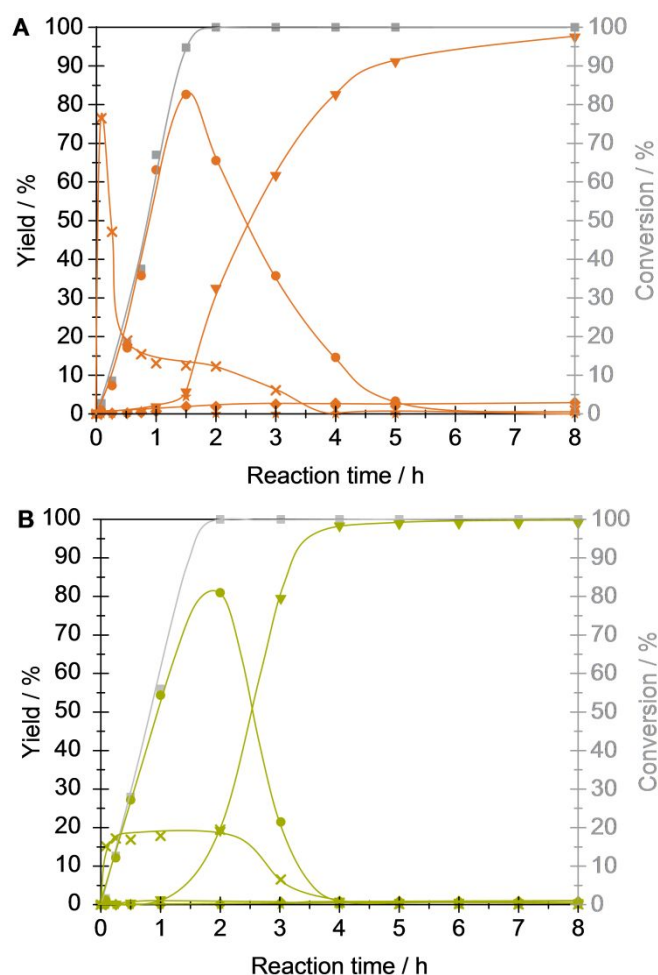

Fig. 9 Product distribution for the hydrodeoxygenation of stearic acid on Ni$_{0.29}$Cu$_{0.71}$/ZrO$_2$, (**A**) and Ni$_{0.59}$Cu$_{0.41}$/ZrO$_2$ (**B**) as a function of time. Conversion of stearic acid (■, ■), yield of 1-octadecanol (●, ●), *n*-heptadecane (▼, ▼), *n*-octadecane (♦, ♦), 1-octadecanal (50 fold) (×, ×) and stearyl stearate (*, *). Reaction conditions: Stearic acid (0.5 g), Ni$_x$Cu$_{1-x}$/ZrO$_2$ catalyst (x = 0.59, 0.29; 0.2 g) (atomic ratio Cu:Ni) *n*-dodecane (100 mL), 260 °C, *p*(H$_2$) = 40 bar, 600 rpm.

Fig. 8 Product distribution for the hydrodeoxygenation of stearic acid on 0.79 Ni/ZrO$_2$ + 0.21 Cu/ZrO$_2$ catalyst (0.2 g), (**A**) and Ni$_{0.79}$Cu$_{0.21}$/ZrO$_2$ (**B**) as a function of time. Conversion of stearic acid (■), yield of 1-octadecanol (●), *n*-heptadecane (▼), *n*-octadecane (♦), 1-octadecanal (50 fold) (×) and stearyl stearate (*). Reaction conditions: Stearic acid (0.5 g), Ni$_x$Cu$_{1-x}$/ZrO$_2$ catalyst (x = 0.79, and respective physical mixture; 0.2 g) (atomic ratio Cu:Ni) *n*-dodecane (100 mL), 260 °C, *p*(H$_2$) = 40 bar, 600 rpm.

By varying the composition of the alloy, different catalytic activities were obtained. High Cu contents (Ni$_{0.29}$Cu$_{0.71}$/ZrO$_2$, **Fig. 9A**) induced higher activity in the reductive deoxygenation, but

The decarbonylation rate depends strongly on the conversion level of stearic acid. Up to 50% of stearic acid conversion, *n*-heptadecane was not formed (**Fig. 8** and **Fig. 9**), although the concentration of 1-octadecanal readily reached the steady state concentration. In this period, the production of 1-octadecanol (Scheme 1/ **a** and **c**) (ESI†, **Fig. S3**) was very selective. Above 50% conversion of stearic acid, the decarbonylation rate increased strongly (**Fig. 10**). The inhibition of decarbonylation by stearic acid (**Fig. 10**) indicates stronger adsorption of stearic acid than of 1-octadecanal on Ni. With pure Ni/ZrO$_2$ the decarbonylation

6 | *Catal. Sci. Technol*., 2019, **00**, 1-3

This journal is © The Royal Society of Chemistry 20xx

rate was low even up to 80% conversion. This is indicative of the competitive adsorption of stearic acid, 1-octadecanol and 1-octadecanal. The coverage of each substance was given in **Eq. S1** to **S2** based on Langmuir type adsorption.

The reaction order with respect to stearic acid reduction was zero (ESI†, **Fig. S4**), the decarbonylation reaction was also zero order in 1-octadecanal (ESI†, **Fig. S5**), but a reaction order of one was observed for conversion of 1-octadecanol (ESI†, **Fig. S6**). Thus, we conclude that the adsorption strength declines from stearic acid via 1-octadecanal to 1-octadecanol. In contrast to Cu/ZrO$_2$ the Ni containing catalysts did not reach equilibrium between 1-octadecanol and 1-octadecanal (ESI†, **Fig. S7**).
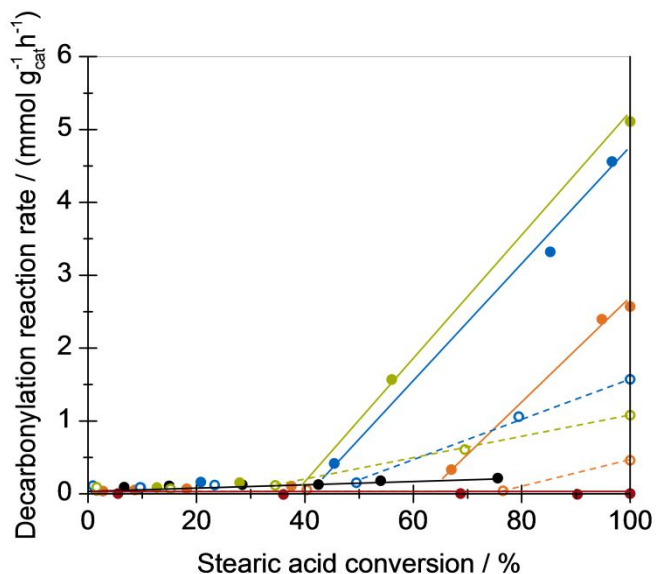
Fig. 10 Decarbonylation reaction rate versus the conversion of stearic acid on Ni$_x$Cu$_{1-x}$/ZrO$_2$ (x = 1, 0.79, 0.59, 0.29, 0) and 0.29 Ni/ZrO$_2$ + 0.71 Cu/ZrO$_2$ as a representative physical mixture. Reaction conditions: Stearic acid (0.5 g), *n*-dodecane (100 mL), 260 °C, *p*(H$_2$) = 40 bar, 600 rpm.

Reduction of stearic acid and decarbonylation of 1-octadecanal on Ni-Cu nano-alloys

To decipher the exceptional high activity of Ni-Cu alloys in the HDO of stearic acid, we next analyze and compare the reaction rate of each individual step leading to *n*-heptadecane, namely reductive deoxygenation of acid (Scheme 1 / **a**) and decarbonylation of 1-octadecanal (Scheme 1 / **b**). The former determines the conversion rate of the fatty acid feedstock while the latter determines the formation rate of the target alkane product. The respective rate equation are formally given by **Eq. S4** to **S6**). Due to the observed reaction order of zero, the rate equation of stearic acid reduction simplifies to **Eq.1**.

$$\frac{dc_{Acid}}{dt} = -k_a n_{cat} \Rightarrow k_a = -\frac{1}{n_{cat}} \frac{dc_{Acid}}{dt}$$

Eq.1

These zero-order reaction rates of fatty acid reduction on Ni$_x$Cu$_{1-x}$/ZrO$_2$ are compared in **Fig. 11**, with those on physical mixtures of Ni/ZrO$_2$ and Cu/ZrO$_2$ as reference. The rates on Ni/ZrO$_2$ were the lowest, having an activation energy (E_a) of 125 kJ mol^{-1} (ESI†, **Fig. S8**). When mixing with Cu/ZrO$_2$, this rate

increased linearly with the Cu content. With incorporation of Cu, the Ni$_{0.79}$Cu$_{0.21}$/ZrO$_2$ and Ni$_{0.59}$Cu$_{0.41}$/ZrO$_2$ had 3.5-fold higher rates than Ni/ZrO$_2$ and also higher activation energy of 135 kJ mol^{-1}. The results imply a change of acid reduction pathways. The OH group of the fatty acid is abstracted by the oxygen defects of ZrO$_2$ on Ni/ZrO$_2$[5a] while this reaction step rather occurs on Cu sites on the bimetallic catalysts. The similarity in rates for Ni$_{0.79}$Cu$_{0.21}$/ZrO$_2$ and Ni$_{0.59}$Cu$_{0.41}$/ZrO$_2$ alloys is speculated to be caused by a similar surface concentration of Cu and Ni in both materials,[12d] implying that, the physical mixtures do not match perfectly with their respective alloy. The rates on the Cu rich alloy Ni$_{0.29}$Cu$_{0.71}$/ZrO$_2$ and Cu/ZrO$_2$ were further doubled to ~12.5 mmol g$_{cat}^{-1}$ h^{-1}, accompanied by a lower activation energy of 107 kJ mol^{-1}, showing that the decreased electron density on Cu lowered the energy barrier of OH abstraction on fatty acid.
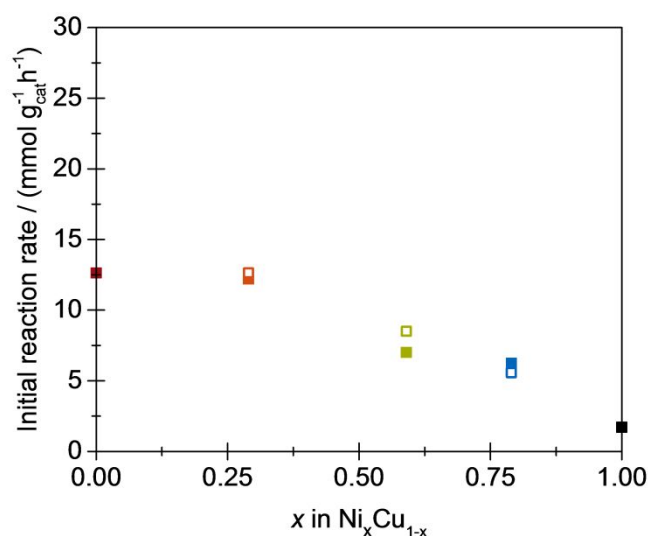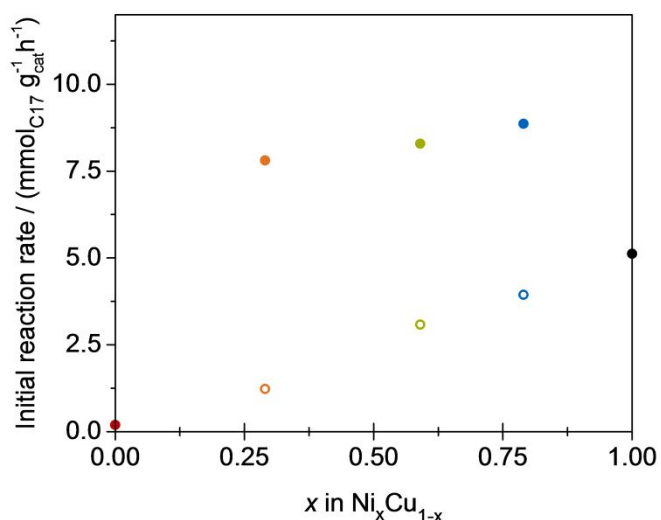

Fig. 11 Initial reaction rate for the reductive deoxygenation of stearic acid on Ni$_x$Cu$_{1-x}$/ZrO$_2$ (x = 1, 0.79, 0.59, 0.29, 0) and physical mixtures of Ni/ZrO$_2$ and Cu/ZrO$_2$ (empty symbols) as a function of Ni content. Reaction conditions: Stearic acid (0.5 g), Ni$_x$Cu$_{1-x}$/ZrO$_2$ catalyst (x = 1, 0.79, 0.59, 0.29, 0; 0.05 g) (atomic ratio Cu:Ni), *n*-dodecane (100 mL), 260 °C, *p*(H$_2$) = 40 bar, 600rpm.

The decarbonylation rate is expressed as *n*-heptadecane formation rate (see **Eq. S7**). When at zero order with respect to 1-octadecanal, the rate can be expressed by (**Eq.2**):

$$\frac{dc_{Hept}}{dt} = n_{cat} k_b \Rightarrow k_b = \frac{1}{n_{cat}} \frac{dc_{Hept}}{dt}$$

Eq.2

This rate increased with Ni content (**Fig. 12**), because Cu was nearly inactive (**Fig. 6**). The nano-alloy Ni$_x$Cu$_{1-x}$/ZrO$_2$ catalysts had much higher rates than Ni/ZrO$_2$, Cu/ZrO$_2$ and their mixture. The TOFs for decarbonylation of 1-octadecanal (TOF, rate normalized to surface Ni) are compiled in **Fig. 13**. Ni/ZrO$_2$ had the lowest TOF values (90 mol$_{C17}$ mol$_{Ni}^{-1}$h^{-1}), while for Ni$_x$Cu$_{1-x}$/ZrO$_2$ TOFs were higher than 460 mol$_{C17}$ mol$_{Ni}^{-1}$h^{-1} (**Fig. 13**). The activation energy decreased from 139 kJ mol^{-1} on Ni/ZrO$_2$ to 130 kJ mol^{-1} on Ni$_{0.79}$Cu$_{0.21}$/ZrO$_2$ and to 121 kJ mol^{-1} over Ni$_{0.29}$Cu$_{0.71}$/ZrO$_2$ (ESI†, **Fig. S9**). The decline in activation energy

This journal is © The Royal Society of Chemistry 20xx

Catal. Sci. Technol., 2019, **00**, 1-3 | **7**

is attributed to the increased electronic density at Ni in the alloy, which we hypothesize to strengthen the interaction with the carbon atom of the carbonyl group and in turn to facilitate the activation of the carbonyl group.[12,13]

Fig. 12 Decarbonylation reaction rate constant on Ni_xCu_{1-x}/ZrO_2 (x = 1, 0.79, 0.59, 0.29, 0) and physical mixtures of Ni/ZrO_2 and Cu/ZrO_2 (empty symbols) as a function of Ni content. Reaction conditions: Stearic acid (0.5 g), Ni_xCu_{1-x}/ZrO_2 or x Ni/ZrO_2 1-x Cu/ZrO_2 (x = 1, 0.79, 0.59, 0.29, 0; 0.2 g) n-dodecane (100 mL), 260 °C, $p(H_2)$ = 40 bar, 600 rpm.
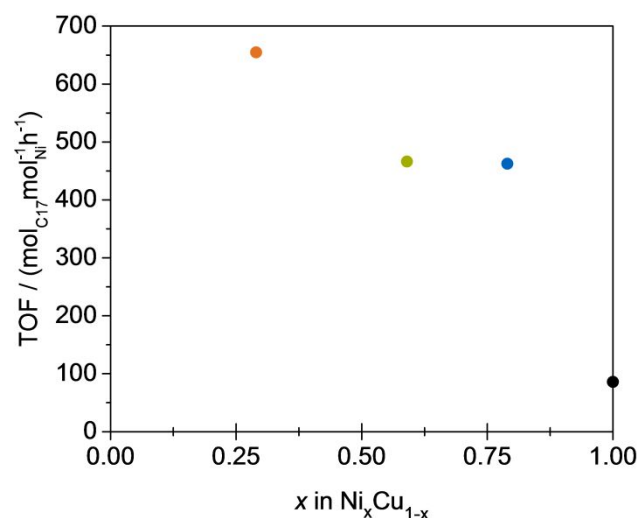
Fig. 13 Turnover frequency of the conversion of 1-octadecanol on Ni_xCu_{1-x}/ZrO_2 (x = 1, 0.79, 0.59, 0.29) as a function of Ni content. Reaction conditions: 1-octadecanol (0.5 g), Ni_xCu_{1-x}/ZrO_2 (x = 1, 0.79, 0.59, 0.29; sum 0.05 g), n-dodecane (100 mL), 260 °C, $p(H_2)$ = 40 bar, stirring at 600 rpm.

Conclusions

The rate of hydrodeoxygenation of stearic acid to n-heptadecane was increased by combining Cu and Ni in a bimetallic catalyst. While Cu/ZrO_2 itself is highly active in the reduction of stearic acid, it hardly catalyzes decarbonylation. In contrast, Ni catalyzes both reactions, albeit with rather low rates.

The reduction of the acid to the aldehyde is followed by decarbonylation. Stearic acid binds stronger than 1-octadecanal on Ni, inhibiting the adsorption of 1-octadecanal and the subsequent decarbonylation. By forming an alloy with Cu the electron density of Ni is increased. This has been unequivocally deduced from the lower binding energy on XPS, and the redshift of the vibration band of linearly adsorbed CO. The increase in electron density strengthened the interaction with the carbonyl group and enhanced the decarbonylation rate. Having both, the high rates of the acid reduction and of the aldehyde decarbonylation, Ni-Cu alloy is a promising catalyst for HDO of stearic acid to alkanes.

Experimental section – Materials and methods

Chemicals All chemicals, i.e., $Zr(OH)_4 \times H_2O$ (XZO 1247/01, MEL Chemicals), $Ni(NO_3)_2 \times 6H_2O$ (Acros Organics, ⩾98.5%), $Cu(NO_3)_2 \times H_2O$ (Sigma-Aldrich, 99.999%), synthetic air (20.5% O_2/ 79.5% N_2, Westfalen), hydrogen (Westfalen, 99.999%), argon (Westfalen, 99.999%), stearic acid (Sigma-Aldrich, ⩾99.5% analytical standard), 1-octadecanol (Sigma-Aldrich, ⩾ 99.5% SelectophoreTM), n-octadecane (Sigma-Aldrich, 99%), n-heptadecane (Sigma-Aldrich, 99%), n-dodecane (Sigma-Aldrich, ⩾ 99%, ReagentPlus), were purchased commercially and were not further purified.

Catalyst preparation The support ZrO_2 material was prepared by calcination of $Zr(OH)_4 \times H_2O$ at 400 °C in ambient air for 4 h (heating rate: 10 °C min^{-1}). Bimetallic Ni_xCu_{1-x}/ZrO_2 catalysts with five different Ni_xCu_{1-x}-ratios (x = 0, 0.29, 0.59, 0.79, 0) and a total metal loading of 8 - 10 wt.% were prepared by wet impregnation. $Ni(NO_3)_2 \times 6H_2O$ and $Cu(NO_3)_2 \times xH_2O$ (Table S1, see SI) were dissolved in deionized H_2O (5.0 g). The resulting solution was added dropwise within half an hour to the support under stirring in ambient air. The slurry was further stirred for 4 h, followed by drying at 110 °C overnight. Subsequently, the ground solid was calcined in synthetic air (flow rate: 100 mL min^{-1}) at 450 °C for 4 h (heating rate: 2 °C min^{-1}) and reduced in H_2 flow (flow rate: 100 mL min^{-1}) at 500 °C for 4 h (heating rate: 2 °C min^{-1}).

Analysis methods

X-Ray powder diffraction (XRD) was performed on a Philips X'Pert Pro and a PANalytical Empyrean System equipped with a Cu Kα radiation source (40 kV/45 mA) with a step size of 0.01711° and a scan rate of 1.08° min^{-1} in the 2θ range of 5−70°; with a step size of 0.0131303° and a scan rate of 0.002205° min^{-1} in the 2θ range of 42−47° using Kα1. Deconvoluted diffraction patterns resulted by subtracting the diffractogram of the ZrO_2-support normalized to the maximum intensity of the m-ZrO_2 peak from the diffractogram of Ni_xCu_{1-x}/ZrO_2 catalyst normalized to the maximum intensity of the m-ZrO_2 peak.

N₂-sorption For measurement of the BET surface area the sample was activated in vacuum at 250 °C for 2 h before measurement. The adsorption of N_2 was performed at −196 °C by using the Sorptiomatic 1990 series instrument.

8 | Catal. Sci. Technol., 2019, **00**, 1-3

This journal is © The Royal Society of Chemistry 20xx

H₂-chemisorption After reduction of the Ni based catalyst samples in H_2-flow at 450 °C for 1 h, they were evacuated at 300 °C for 1 h. The H_2 adsorption isotherms accounting for both chemisorption and physisorption were measured on a Thermo Scientific's Surfer instrument at a pressure ranging from 9 to 400 mbar at 25 °C. For removing physisorbed H_2 the system was evacuated for 20 min afterwards. By extrapolating the isotherm to zero H_2 pressure the concentration of chemisorbed hydrogen on the metal was determined. The Ni dispersion was derived by assuming an average surface Ni to H ratio of 1. Furthermore, it is assumed that Cu does not chemisorb H_2.[22]

Temperature programmed desorption (TPD) of ammonia and carbon dioxide was carried out in a parallel reactor system (six fold). A prior activation of the pressed samples (500–710 μm) in He at 500 °C for 1 h was conducted. Consequently, the sample was evacuated at 10^{-2} mbar the adsorbent NH_3 or CO_2 was loaded at a partial pressure of 1 mbar and 100 °C or 40 °C, respectively. The sample was then purged with He for 1 h in order to remove physisorbed molecules. After activation, the six samples were heated from 100 to 770 °C with a rate of 10 °C min^{-1} to desorb NH_3 and from 40 to 700 °C to desorb CO_2. The signals were detected by a Balzer QME 200 mass spectrometer. For calibration purposes NH_3 was desorbed from a HMFI-90 standard and CO_2 generation from $NaHCO_3$ decomposition was used for CO_2 calibration.

Atomic absorption spectroscopy (AAS) was used to determine the Ni and Cu content of the catalysts with a ThermoFisher Solaar M5 AA-Spectrometer. Prior to Ni and Cu determination, the catalysts were dissolved in a mixture of HF, HNO_3 and boiling concentrated H_2SO_4.

IR spectroscopy of adsorbed CO was performed on a Bruker VERTEX 70 spectrometer at a resolution of 2 cm^{-1} with 128 scans in the range of 1000-4000 cm^{-1}. For the measurements, the samples were pressed in to self-supporting wafers and mounted in the sample holder. The Ni-Cu/ZrO_2 catalysts were activated in H_2-flow at 450 °C for 1 h, and then subsequently outgassed under vacuum ($p = 10^{-7}$ mbar) to remove H_2 while cooling to 40 °C. The adsorption of CO was performed at 0.3 mbar until equilibrium was reached, then evacuated ($p = 10^{-7}$ mbar) for 5 min to remove physisorbed and gas phase CO. The IR spectra of adsorbed CO were obtained by subtracting the activated sample, and then were normalized by the weight of the Ni in the respective wafer.

EDS analysis Imaging and EDS mapping was performed with Scanning Transmission Electron Microscope (STEM) (JEOL JEM-ARM200F) operated at 200 kV. The microscope houses aberration corrector for the probe forming lens (CEOS GmbH double-hexapole aberration corrector), which allows imaging with sub angstrom resolution. The presented images were acquired on HAADF detector, with beam convergence of 27.5 mrad and collection angle of 68-280 mrad. Elemental analysis was performed using Energy Dispersive X-ray Spectroscopy (EDS) using high collection angle SSD. (~0.7 srad, JEOL Centurio). Acquisition and evaluation of the spectra was performed by NSS Thermo Scientific software package. The STEM sample preparation involved mounting of the powder samples on Au grids coated with lacey carbon support films, and then immediately loading them into the STEM airlock to minimize an exposure to atmospheric O_2.

XPS analysis The respective material was pressed to achieve a self-supporting pellet. These were reduced (10°C min^{-1}, 100 mL min^{-1} 5 vol.% H_2 in N_2, 500°C, 1 h), cooled to ambient temperature and were transferred to a glove box, placed in a pressurized vessel and loaded into the XPS under N_2 atmosphere. XPS was measured with a monochromated Al K_α source using a low energy flood gun for charge compensation. The binding energy scale was calibrated to the $Zr_{3d5/2}$ peak.[29] Ni metal peaks were fit with an asymmetric line shape, while Cu metal peaks and Ni-O peaks were fit using a Gaussian-Lorentzian line shape using CasaXPS.

Catalyst activity and kinetic measurement
For catalytic reactions an autoclave (Parr, 300 mL) was used. Stearic acid or 1-octadecanol, catalyst, and 100 mL n-dodecane were loaded into the autoclave, and pressurized with H_2 (3 × 20 bar). Typically, the reaction was carried out at 260 °C in the presence of 40 bar H_2 at a stirring speed of 600 rpm. *In situ* sampling was performed during the reaction. Typically, each sample of max. 0.5 mL was withdrawn from the reaction slurry and filtered through a 2 μm filter at the bottom of the reactor in order to make sure that the sample is free of catalyst, that the reaction in the sample vial is stopped and that the mass of catalyst in the reactor stays constant. The dead volume between filter and end of the sampling tube (0.05 mL) was flushed and discarded prior to every sampling. The liquid samples were analyzed by a Agilent 7890B GC system, equipped with a flame ionization detector (FID) and Agilent 5977 MS detector, using a HP-5 capillary column (30 m, 0.32 mm inner diameter, 0.25 μm film). Quantification error is less than 5% for all experiments.
Conversion = (weight of converted reactant / weight of the starting reactant) × 100%. **Yield** (C%) = (C atoms in each product / C atoms in the starting reactant) × 100%. **Selectivity** (C%) = (C atoms in each product/sum of C atoms in all the products) × 100%. The **initial reaction rate** was deduced from the slope of the linear fit to the conversion *versus* time plot in the linear region at low conversions (<20%). **Rate** = mole of converted reactant / reaction time. **TOF** = rate / mole of accessible Ni on the catalyst's surface = mole of converted reactant / mole of accessible Ni on the catalyst's surface / reaction time. The apparent activation barrier $E_{a(app)}$ was determined regarding an Arrhenius plot for the reaction of stearic acid to 1-octadecanol. The **enthalpy of activation** and **entropy of activation** for the decarbonylation is determined by the Eyring equation. Only in the latter case, the determination of the TOF was possible, since this reaction is only occurring on Ni sites. The respective figures are given in (ESI†, **Fig. S9**) and (ESI†, **Fig. S10**). The **decarbonylation reaction rate** of 1-octadecanal is calculated based on the increase of heptadecane yield within a specific time. Rate(decarbonylation) = ΔYield(heptadecane) / ΔTime.

Conflicts of interest

There are no conflicts to declare.

This journal is © The Royal Society of Chemistry 20xx

Catal. Sci. Technol., 2019, **00**, 1-3 | **9**

Acknowledgements

References

1   (a) J. Jakkula, V. Niemi, J. Nikkonen, V.-M. Purola, J. Myllyoja, P. Aalto, J. Lehtonen and V. Alopaeus, Neste Oil Oyj, EP1396531 B1, **2007**; (b) E. Furimsky, *Catal. Rev.*, 1983, **25**, 421–458.

2   (a) M. Snåre, I. Kubičková, P. Mäki-Arvela, K. Eränen and D. Y. Murzin, *Ind. Eng. Chem. Res.*, 2006, **45**, 5708–5715; (b) M. Snåre, I. Kubičková, P. Mäki-Arvela, D. Chichova, K. Eränen and D. Y. Murzin, *Fuel*, 2008, **87**, 933–945; (c) J. G. Immer, M. J. Kelly and H. H. Lamb, *Appl. Catal. A*, 2010, **375**, 134–139.

3   (a) S. A. W. Hollak, R. W. Gosselink, D. S. van Es and J. H. Bitter, *ACS Catal.*, 2013, **3**, 2837–2844; (b) R. W. Gosselink, D. R. Stellwagen and J. H. Bitter, *Angew. Chem. Int. Ed.*, 2013, **52**, 5089–5092.

4   (a) B. Peng, X. Yuan, C. Zhao and J. A. Lercher, *J. Am. Chem. Soc.*, 2012, **134**, 9400–9405; (b) B. Peng, Y. Yao, C. Zhao and J. A. Lercher, *Angew. Chem. Int. Ed.*, 2012, **51**, 2072–2075.

5   (a) S. Foraita, J. L. Fulton, Z. A. Chase, A. Vjunov, P. Xu, E. Baráth, D. M. Camaioni, C. Zhao and J. A. Lercher, *Chem. Eur. J.*, 2015, **21**, 2423–2434; (b) B. Peng, C. Zhao, S. Kasakov, S. Foraita and J. A. Lercher, *Chem. Eur. J.*, 2013, **19**, 4732–4741; (c) R. Pestman, A. van Duijne, J. A. Z. Pieterse and V. Ponec, *J. Mol. Catal. A Chem.*, 1995, **103**, 175–180; (d) C. Zhao, T. Brück and J. A. Lercher, *Green Chem.*, 2013, **15**, 1720–1739.

6   (a) D. M. Alonso, S. G. Wettsteinab and J. A. Dumesic, *Chem. Soc. Rev.*, 2012, **41**, 8075–8098; (b) J. Lee, Y. T. Kim and G. W. Huber, *Green Chem.*, 2014, **16**, 708–718; (c) M. Toba, S. Tanaka, S. Niwa, F. Mizukami, Z. Koppány, L. Guczi, K.-Y. Cheah and T.-S. Tang, *Appl. Catal. A*, 1999, **189**, 243–250; (d) B. Rozmysłowicz, A. Kirilin, A. Aho, H. Manyar, C. Hardacre, J. Wärnå, T. Salmi and D. Y. Murzin, *J. Catal.*, 2015, **328**, 197–207; (e) H. G. Manyar, C. Paun, R. Pilus, D. W. Rooney, J. M. Thompson and C. Hardacre, *Chem. Commun.*, 2010, **46**, 6279–6281.

7   S. Foraita, Y. Liu, G. H. Haller, E. Baráth, C. Zhao and J. A. Lercher, *ChemCatChem*, 2017, **9**, 195–203.

8   (a) G. W. Huber, S. Iborra and A. Corma, *Chem. Rev.*, 2006, **106**, 4044–4098; (b) M. A. N. Santiago, M. A. Sánchez-Castillo, R. D. Cortright and J. A. Dumesic, *J. Catal.*, 2000, **193**, 16–28; (c) T. Turek, D. L. Trimm and N. W. Cant, *Catal. Rev.: Sci. Eng.*, 1994, **36**, 645–683; (d) K. Kandel, J. W. Anderegg, N. C. Nelson, U. Chaudhary and I. I. Slowing, *J. Catal.*, 2014, **314**, 142–148.

9   K. Kandel, C. Frederickson, E. A. Smith, Y. J. Lee and I. I. Slowing, *ACS Catal.*, 2013, **3**, 2750–2758.

10 K. Kandel, U. Chaudhary, N. C. Nelson and I. I. Slowing, *ACS Catal.*, 2015, **5**, 6719–6723.

11 (a) X. R. Li, C. Zhang, H. Y. Cheng, L. M. He, W. W. Lin, Y. C. Yu and F. Y. Zhao, *J. Mol. Catal. A Chem.*, 2014, **395**, 1–6; (b) X. R. Li, C. Zhang, H. Y. Cheng, W. W. Lin, P. J. Chang, B. Zhang, Q. F. Wu, Y. C. Yu and F. Y. Zhao, *ChemCatChem*, 2015, **7**, 1322–1328; (c) B. Mallesham, P. Sudarsanam and B. M. Reddy, *Ind. Eng. Chem. Res.*, 2014, **53**, 18775–18785; (d) W. Sun, Y. Song, X. Q. Gong, L. M. Cao and J. Yang, *Chem. Sci.*, 2015, **6**, 4993–4999; (e) R. Ding, Y. Wu, Y. Chen, H. Chen, J. Wang, Y. Shi and M. Yang, *Catal. Sci. Technol.*, 2016, **6**, 2065–2076.

12 (a) A. van der Burg, J. Doornbos, N. J. Kos, W. J. Ultee and V. Ponec, *J. Catal.*, 1978, **54**, 243–253; (b) F. J. C. M. Toolenaar, F. Stoop and V. Ponec, *J. Catal.*, 1983, **82**, 1–12; (c) J.-A. Dalmon, M. Primet, G.-A. Martin and B. Imelik, *Surface Science*, 1975, **50**, 95–108. (d) V. Ponec, *Surf. Sci.* 1979, **80**, 352–366

13 (a) N. Iwasa, M. Takizawa and M. Arai, *Appl. Catal. A*, 2005, **283**, 255–263; (b) D. Wang, F. Ammari, R. Touroude, D. S. Su and R. Schlögl, *Catal. Today*, 2009, **147**, 224–230; (c) M. Consonni, D. Jokic, D. Yu Murzin and R. Touroude, *J. Catal.*, 1999, **188**, 165–175.

14 (a) H. Adkins and K. Folkers, *J. Am. Chem. Soc.*, 1931, **53**, 1095–1097; (b) D. S. Brands, E. K. Poels and A. Bliek, *Appl. Catal. A*, 1999, **184**, 279–289; (c) T. Voeste and H. Buchold, *J. Am. Oil Chem. Soc.*, 1984, **61**, 350–352; (d) T. Turek, D. L. Trimm and N. W. Cant, *Catal. Rev.: Sci. Eng.*, 1994, **36**, 645–683; (e) C. J. G. van de Grift, A. F. H. Wielers, B. P. J. Joghi, J. van Beijnum, M. de Boer, M. Versluijs-Helder and J. W. Geus *J. Catal.*, 1991, **131**, 178–189; (f) F. T. van de Scheur, B. van de Linden, M. Mittelmeijer-Hazeleger, J. G. Nazloomian and L. H. Staal, *Appl. Catal. A*, 1994, **111**, 63–77.

15 W. Song, C. Zhao and J. A. Lercher, *Chem. Eur. J.*, 2013, **19**, 9833–9842.

16 (a) R. G. Kukushkin, O. A. Bulavchenko, V. V. Kaichev and V. A. Yakovlev, *Appl. Catal. B*, 2015, **163**, 531–538; (b) A. A. Smirnov, S. A. Khromova, O. A. Bulavchenko, V. V. Kaichev, A. A. Saraev, S. I. Reshetnikov, M. V. Bykova, L. I. Trusov and V. A. Yakovlev, *Kinet. Catal.*, 2014, **55**, 69–78; (c) S. Zavarukhin, V. Yakovlev, V. Parmon, V. Sister, E. Ivannikova and O. Eliseeva, *Chem. Technol. Fuels Oils*, 2010, **46**, 1–8; (d) V. O. Dundich, S. A. Khromova, D. Y. Ermakov, M. Y. Lebedev, V. M. Novopashina, V. G. Sister, A. I. Yakimchuk and V. A. Yakovlev, *Kinet. Catal.*, 2010, **51**, 704–709.

17 D. M. Alonso, S. G. Wettstein and J. A. Dumesic, *Chem. Soc. Rev.*, 2012, **41**, 8075–8098.

18 (a) R. Pestman, R. M. Koster, J. A. Z. Pieterse and V. Ponec, *J. Catal.*, 1997, **168**, 255–264; (b) R. Pestman, R. M. Koster, A. van Duijne, J. A. Z. Pieterse and V. Ponec *J. Catal.*, 1997, **168**, 265–272.

19 K. Tanabe, *Mater. Chem. Phys.*, 1985, **13**, 347–364.

20 (a) W. Li, H. Huang, H. Li, W. Zhang and H. Liu, *Langmuir*, 2008, **24**, 8358–8366; (b) H. K. Schmid, *J. Am. Ceram. Soc.*, 1987, **70**, 367–376.

21 (a) B. Bachiller-Baeza, I. Rodriguez-Ramos and A. Guerrero-Ruiz, *Langmuir*, 1998, **14**, 3556–3564; (b) Z. Wang, Y. Jiang, M. Hunger, A. Baiker and J. Huang, *ChemCatChem*, 2014, **6**, 2970–2975; (c) Y. Zhao, W. Li, M. Zhang and K. Tao, *Catal. Commun.*, 2002, **3**, 239–245.

22 A. Kitla, O. V. Safonova and K. Foettinger, *Catal. Lett.*, 2013, **143**, 517–530.

23 E. T. Saw, U. Oemar, X. R. Tan, Y. Du, A. Borgna, K. Hidajat and S. Kawi, *J. Catal.*, 2014, **314**, 32–46.

24 A. Bandara, S. Dobashi, J. Kubota, K. Onda, A. Wada, K. Domen, C. Hirose and S. S. Kano, *Surf. Sci.*, 1997, **387**, 312–319.

25 I. R. Harris, I. L. Dillamore, R. E. Smallman and B. E. P. Beeston, *Philos. Mag.*, 1966, **14**, 325–333.

26 (a) G. Blyholder, *J. Phys. Chem.*, 1964, **68**, 2772–2778; (b) M. Gajdoš, A. Eichler and J. Hafner, *J. Phys. Condens. Matter.*, 2004, **16**, 1141–1164.

27 B. Hernnas, M. Karolewski, H. Tillborg, A. Nilsson and N. Martensson, *Surf. Sci.*, 1994, **302**, 64–72.

28 K. P. Kepp, *Inorg. Chem.* 2016, **55**, 9461–9470.

29   J. A. Anderson and J. L. G. Fierro, *J. Solid State Chem.*, 1994, **108**, 305–313.

29   J. A. Anderson and J. L. G. Fierro, *J. Solid State Chem.*, 1994, **108**,

This journal is © The Royal Society of Chemistry 20xx

Catal. Sci. Technol., 2019, **00**, 1-3 | **11**

TOC – For graphical use only
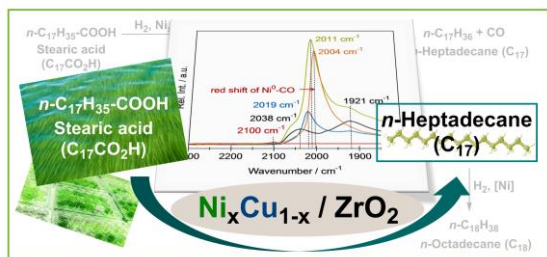
The combination of Cu and Ni in bimetallic catalysts on ZrO$_2$, lead to a more efficient HDO of stearic acid.